

FAST AND OPTIMAL CMB LENSING USING STATISTICAL INTERPOLATION ON THE SPHERE

GUILHEM LAVAUX

Department of Physics, University of Illinois at Urbana-Champaign, 1002 W Green St, Urbana, IL, 61801, USA

BENJAMIN D. WANDELT

Institut d'Astrophysique de Paris, UMR 7095 CNRS-Université Pierre et Marie Curie, 98bis bd Arago, F-75014 Paris, FRANCE and
Department of Physics, University of Illinois at Urbana-Champaign, 1002 W Green St, Urbana, IL, 61801, USA

(Dated: September 17, 2018)
Draft version September 17, 2018

ABSTRACT

We describe a accurate and fast pixel-based statistical method to interpolate fields of arbitrary spin on the sphere. We call this method Fast and Lean Interpolation on the Sphere (FLINTS). The method predicts the optimal interpolated values based on the theory of isotropic Gaussian random fields and provides an accurate error estimate at no additional cost. We use this method to compute lensed Cosmic Microwave Background (CMB) maps precisely and quickly, achieving a relative precision of 0.02% at a HEALPIX resolution of $N_{\text{side}} = 4,096$, for a bandlimit of $\ell_{\text{max}} = 4,096$ in the same time it takes to simulate the original, unlensed CMB map. The method is suitable for efficient, distributed memory parallelization. The power spectra of our lensed maps are accurate to better than 0.5% at $\ell = 3,000$ for the temperature, the E and B mode of the polarization. As expected theoretically, we demonstrate that, on realistic cases, this method is between two to three orders of magnitude more precise than other known interpolation methods for the same computational cost.

1. INTRODUCTION

Gravitational lensing of the Cosmic Microwave Background (CMB) is a unique probe of the distribution of mass in the entire visible Universe. The first signatures of this CMB lensing signal have already been seen in cross-correlation with large scale structure templates (Smith et al. 2007; Hirata et al. 2008). The effect of lensing on the CMB power spectra will provide powerful additional constraints on the physics of the dark sector (Abazajian & Dodelson 2003; Smith et al. 2006a). Including reconstruction of the lensing potential in cosmological parameter analysis removes further degeneracies. Once the lensing deflection is mapped with high precision it will likely allow detecting the absolute mass scale of neutrinos (Kaplinghat et al. 2003; Lesgourgues et al. 2006) and provide tight constraints on the presence of dark energy at redshifts $z \sim 2$. Lensing creates polarization B modes by rotating the stronger E modes (Zaldarriaga & Seljak 1997). These lensing B modes are not affected by cosmic variance and can therefore significantly improve reconstructions of the lensing potential (Smith et al. 2006b). The modeling of lensing B modes is further motivated since they are a foreground for the search for the B -mode signal of inflationary gravitational waves (Knox & Song 2002; Kesden et al. 2002).

PLANCK will yield the first all-sky temperature and polarization maps of the CMB with sufficient signal to noise to detect this signal. Ground based experiments such as QUBIC (Hamilton & Charlassier 2010), SPT-pol (McMahon et al. 2009) or QUIET (Newburgh et al. 2005) contain detailed information about the fine-scale structure imprinted by lensing while still covering significant portions of the sky. For the extraction of lensing and polarization science from these data sets, fast and precise methods to simulated lensed all-sky CMB maps are indispensable.

In the Born approximation, which specifies that the lensing effects may be modeled by the impact of a single lens plane on the CMB, the lensing corresponds to looking up at the value of the temperature or the polarization at displaced position on the sky. Thus, making lensed maps is effectively a resampling of the CMB on a different set of positions. Different technical solutions were proposed. Currently three main techniques are known.

The first technique consists in doing a brute force resummation of the spherical harmonics at a new set of positions. Acceleration methods using symmetry properties of the sampling positions can not be used. While prohibitively expensive for practical use, this method is exact and we therefore employ it on a subset of pixels as a precision benchmark for other methods.

The second technique is polynomial interpolation on the sphere to compute the value of the temperature and polarization field at the displaced positions. The most simple of the interpolation technique is a bilinear interpolation of fields on the sphere (hereafter called the naive technique). Another algorithm, a Lagrange polynomial interpolation on the Equi-cylindrical Projection, was first proposed by Hirata et al. (2004) and then later used by Das & Bode (2008) for a full-sky simulation of the CMB lensing on a light cone of a cosmological simulation. A variant of this method, involving a bicubic interpolation scheme, is implemented in the publicly available code LENSPIX¹ described in Lewis (2005) and Hamimeche & Lewis (2008) (hereafter the ECP algorithm).

A third technique has been recently developed by Basak et al. (2009). This algorithm consists in recasting the spherical harmonic coefficient of the unlensed field into the Fourier basis in the (θ, ϕ) variables. Then,

¹ <http://cosmologist.info/lenspix>

we may use a Non-equispaced Fast Fourier Transform (NFFT) to compute the field at the displaced positions. This method achieves high precision and is significantly faster than the first technique though still too slow to allow for the production of a large set of lensed maps, which is required for the statistical analysis of observed CMB data.

We propose a fourth technique that relies on the statistical properties of the considered fields to be lensed. It is based on the idea of interpolating the original field but using the known spectral information to compute the correct weighing coefficients for the interpolation. This method is related to a Wiener filter (Wiener 1949) but not limited to pure Gaussian random field. We call this method Fast and Lean Interpolation on the Sphere (FLINTS).² In this work, we analyze the result obtained based on a HEALPIX pixelization. We note that our framework may be used on any pixelization of the sphere, including the Equi-cylindrical projection already used in previous works. The implementation that we propose takes advantage of the geometrical properties of HEALPIX for a number of memory and computational optimizations.

We note that our interpolation method is of general interest beyond its application to lensing. In fact, since it is based on Wiener filtering it is guaranteed to give the best possible mean squared error of any method for a field with the same power spectrum and for fixed interpolation stencil.

The structure of this paper is the following. In Section 2, we describe the general interpolation method. Then, in Section 3, we discuss its performance in generating lensed CMB maps. In Section 4, we conclude.

2. INTERPOLATING CMB FLUCTUATIONS

We propose a direct, simple though sufficiently precise method of interpolating complex fields on the sphere. This method is based on the most likely value an isotropic Gaussian random field takes at an arbitrary location on the sphere, given a set of sampled values (the interpolation stencil) and its power spectrum C_l . In Section 2.1, we study the general method for the special case of spin-0 fields. Then, we generalize the obtained equations to spin- s fields in Section 2.2. We then detail in Section 2.3 the algorithmic steps used to compute the identifiers of the pixels that are used in the interpolation. In Section 2.4, we describe the memory and computational time optimizations that we used in FLINTS. We then list all the steps required to achieve the interpolation in Section 2.5. Finally, in Section 2.6, we discuss the results of the raw performance tests of our interpolation method.

2.1. Interpolating a scalar field

We start by considering a Gaussian random scalar field on the sphere given by the function $T(\hat{n})$, in the direction \hat{n} . The general form of the joint probability of the value

of $T(\hat{n})$ in $N + 1$ directions is:

$$\mathcal{P}(T(\hat{n}_0), T(\hat{n}_1), \dots, T(\hat{n}_N)) = \frac{\sqrt{|\det W|}}{(2\pi)^{(N+1)/2}} \exp\left(-\frac{1}{2\sigma_0^2} \sum_{i,j=0}^N W_{i,j} T(\hat{n}_i) T(\hat{n}_j)\right). \quad (1)$$

with W the inverse of the correlation matrix being

$$W = V^{-1}, \quad (2)$$

with $V_{i,j}$ defined for two directions \hat{n}_i and \hat{n}_j as

$$V_{i,j} = \frac{1}{\sigma_0^2} \zeta(\hat{n}_i \cdot \hat{n}_j), \quad (3)$$

with the correlation function $\zeta(\cos\theta)$ for two directions separated by an angle θ

$$\zeta(\cos\theta) = \sum_{\ell=1}^{\ell_{max}} \left(\frac{2\ell+1}{4\pi}\right) C_\ell P_\ell(\cos\theta), \quad (4)$$

and the intrinsic variance of the temperature field

$$\sigma_0^2 = \zeta(\cos(0) = 1). \quad (5)$$

Now, we can compute the conditional probability of the value of $T(\hat{n}_0)$ given the N other values:

$$\mathcal{P}(T(\hat{n}_0)|T(\hat{n}_1), \dots, T(\hat{n}_N)) = \frac{\sqrt{W_{0,0}}}{2\pi} \exp\left(-\frac{W_{0,0}}{2}(T(\hat{n}_0) - \bar{T})^2\right), \quad (6)$$

with

$$\bar{T} = W_{0,0}^{-1} \sum_{i=1}^N W_{0,i} T(\hat{n}_i), \quad (7)$$

and $W_{0,0}$ the top-left most element of the W matrix. So, given the values in the directions $\{\hat{n}_1, \dots, \hat{n}_N\}$, we define the interpolated value in the direction \hat{n}_0 to be equal to the most likely value \bar{T} as defined above. The precision of the interpolation is given by the amount of allowed fluctuation $1/\sqrt{W_{0,0}}$. The advantage of this procedure is that it is flexible in the number of points we take into account for the interpolation. Additionally, it remains purely local and the complexity scales as $O(N^2 \times N_{\text{pix}})$, with N the number of points to compute the interpolation and N_{pix} the number of pixels in the map. This locality allows us to take full advantage of the parallelism offered by current multi-core CPUs and by distributed computing environments. An illustration of our interpolation procedure is given Fig. 1 for the case of interpolation stencil with 9 elements ("neighbours").

We further increase the speed of the interpolation by precomputing the covariance matrix linked to the pixelization, that is the inverse of the matrix $S_{i,j}$ defined by:

$$S_{i,j} = \frac{1}{\sigma_0^2} \langle T(\hat{n}_i) T(\hat{n}_j) \rangle \quad (8)$$

for \hat{n}_i the direction corresponding to the center of a pixel of the map to be interpolated. Strictly speaking, we would need to recompute these matrices if the angular power spectrum of temperature fluctuations changes.

² The reference implementation is written in C++/OpenMP and is available at <http://www.iap.fr/users/lavaux/flints.php>.

But as the weights are continuous functions of the angular power spectra, two relatively similar spectra should give the same weights. This alleviates the need of recomputing these weights for any single change of the angular power spectra, at the potential cost of a small loss of precision. $S_{i,j}$ is in practice a 9×9 matrix as we have nine neighbors for any direction of interpolation. Once we have this matrix it is fast to determine the $W_{0,i}$ by doing block matrix computation (Press et al. 1992). First, we write the shape of the V matrix:

$$V = \begin{pmatrix} 1 & B^T \\ B & S \end{pmatrix}. \quad (9)$$

We let the block matrix shape of its inverse W have the following shape

$$W = \begin{pmatrix} 1/\tilde{\sigma}_0^2 & \tilde{B}^T \\ \tilde{B} & \tilde{S} \end{pmatrix} \quad (10)$$

and write that the product should make identity:

$$V \times W = \begin{pmatrix} \left(\frac{1}{\tilde{\sigma}_0^2} + B^T \tilde{B} \right) & \left(\tilde{B}^T + B^T \tilde{S} \right) \\ \left(\frac{B}{\tilde{\sigma}_0^2} + S \tilde{B} \right) & \left(B \tilde{B}^T + S \tilde{S} \right) \end{pmatrix}, \quad (11)$$

which leads us to the following equalities:

$$\tilde{\sigma}_0^2 = (1 - B^\dagger S^{-1} B), \quad (12)$$

$$\tilde{B} = -\frac{1}{\tilde{\sigma}_0^2} S^{-1} B, \quad (13)$$

$$\tilde{S} = \frac{1}{\tilde{\sigma}_0^2} S^{-1} B B^\dagger S^{-1}. \quad (14)$$

The matrix \tilde{S} gives the correlation between the different direction of the pixelization, \tilde{B} gives the correlation between the sought interpolated direction and the direction of the pixelization, $\tilde{\sigma}_0$ is the standard deviation of the interpolator in the interpolated direction. The equations (12) and (13) are computed as needed for each interpolated direction. The equation (14) is not used as we do not need this part of the matrix.

Finally, we may express the value of the temperature in the interpolated direction \hat{n} :

$$\bar{T}(\hat{n}) = \sum_{i,j=1}^N S_{i,j}^{-1} \frac{\langle T(\hat{n}) T(\hat{n}_j) \rangle}{\sigma_0^2} T(\hat{n}_i), \quad (15)$$

for which the Gaussian variance of the error of this estimator is

$$\sigma_T^2(\hat{n}) = \sigma_0^2 \left(1 - \frac{1}{\sigma_0^4} \sum_{i,j=1}^N S_{i,j}^{-1} \langle T(\hat{n}) T(\hat{n}_i) \rangle \langle T(\hat{n}) T(\hat{n}_j) \rangle \right). \quad (16)$$

The above Eq. (15) is the strict equivalent of Eq. (7). We now have both an interpolated value and an estimate of the interpolation error. Even though we used a Gaussian field theory to derive these estimators, the interpolation is also optimal in a least-squared sense for non-Gaussian field.

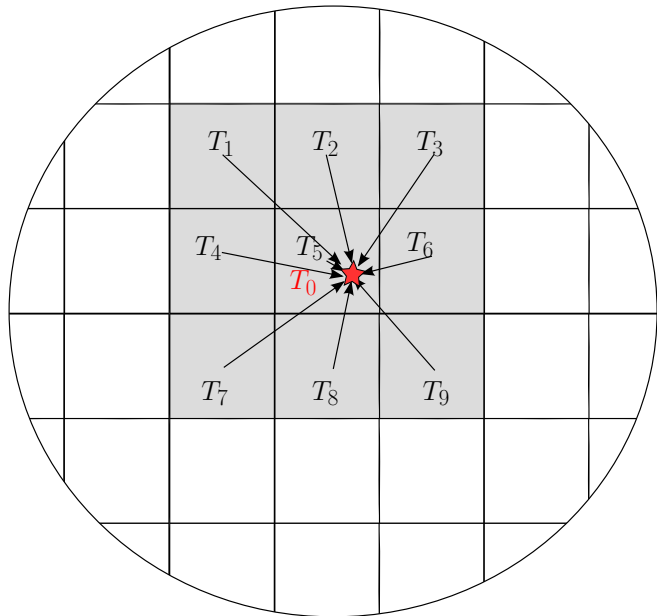


Figure 1. *Illustration of our interpolation procedure* – We present here an illustration of the procedure. To get the value of the field interpolated at the position illustrated by the red star, we use the value of this field sampled on the grid given by the squares. In this setting only the nine nearest neighbors, with temperature value T_i , contribute to the value T_0 .

The time complexity of a HEALPIX spherical harmonic transform (Górski et al. 2005) is $O(N_{\text{side}} \ell_{\text{max}}^2)$, with ℓ_{max} the number of ℓ modes used for the spherical harmonic transform. The difference in complexity between the HEALPIX spherical harmonic transform and our method means that if the number of neighbors N is sufficiently small then our method would be faster to compute a complete CMB sky in any direction than generating a very high resolution HEALPIX map. This improvement may be of order $O(\ell_{\text{max}}^2 / (N^2 N_{\text{side,high}}))$ for large ℓ_{max} , where $N_{\text{side,high}}$ is the high resolution map needed for the naive technique.

We note that, in the high resolution regime, the scaling of this algorithm is like the one of the ECP technique (Hirata et al. 2004; Hamimeche & Lewis 2008). On the other hand, there are several advantages to our procedure. First, the method provides an accurate error estimate for no additional computational cost. The weights take into account the part of the signal which is not well represented by the pixelization. The ECP interpolation implicitly assume that all the information is stored completely in a neighborhood of the direction of interpolation, whereas our interpolation takes into account the possible lack of complete information. Second, FLINTS does not need another specific spherical harmonic transform to generate the lensed fluctuation on the sphere. It may use a previously existing or independently generated map.

2.2. Interpolating spin- s fields

We may now adapt our method for the case of spin- s fields on the sphere. The concepts are the same, except that we must now handle complex fields. We want to interpolate the complex field $P(\hat{n})$. We assume that this field is isotropic and its correlation function is defined

by:

$$\begin{aligned}
\langle P^*(\hat{n}')P(\hat{n}) \rangle &= \sum_{l=s}^{+\infty} \sqrt{\frac{2l+1}{4\pi}} C_{P,l}({}_s Y_{l,-s}(\beta, \alpha)) e^{-is\gamma} \quad (17) \\
&= \sum_{l=s}^{+\infty} \left(\frac{2l+1}{4\pi} \right) C_{P,l} d_{-s,-s}^l(\beta) e^{-is(\gamma+\phi)} \quad (18) \\
&= {}_s \zeta(\alpha, \beta, \gamma), \quad (19)
\end{aligned}$$

with α, β, γ the Euler angles defining the rotation to transform \hat{n}' into \hat{n} and ${}_s Y_{l,m}$ the spin s spherical harmonic (see Appendix A for the definition).

The function $d_{-s,-s}^l$ is the Wigner d function. An algorithm to compute this function is recalled in Appendix B, and has already been detailed in Trapani & Navaza (2006). An illustration that defines more properly these angles is given in Fig. 2.

As in Eq. (3), we define the Hermitian correlation matrix for two directions \hat{n}_i and \hat{n}_j , $0 \leq i, j \leq N$:

$$V_{i,j} = \frac{{}_s \zeta(\alpha_{i,j}, \beta_{i,j}, \gamma_{i,j})}{{}_s \zeta(0, 0, 0)}, \quad (20)$$

with $\alpha_{i,j}$, $\beta_{i,j}$ and $\gamma_{i,j}$ the Euler angles defining the rotation to transform \hat{n}_i in \hat{n}_j . Similarly as in Eq. (9), we define the Hermitian matrix S corresponding to the correlation of the values taken by the HEALPIX pixels, which corresponds here to the indices $1 \leq i, j \leq N$.

Using some geometry on the sphere it is possible to compute the above angles. The relation between $\hat{n}'(\theta', \phi')$, $\hat{n}(\theta, \phi)$ and (α, β, γ) is given by:

$$\cos \beta = \hat{n} \cdot \hat{n}', \quad (21)$$

$$\beta > 0, \quad (22)$$

$$\cos \alpha = -\frac{(\sin \theta \cos \theta' \cos(\phi - \phi') - \cos \theta \cos \theta')}{\sin \beta}, \quad (23)$$

$$\sin \alpha = \frac{\sin \theta}{\sin \beta} \sin(\phi' - \phi), \quad (24)$$

$$\cos \gamma = -\frac{(\sin \theta' \cos \theta \cos(\phi - \phi') - \cos \theta' \cos \theta)}{\sin \beta}, \quad (25)$$

$$\sin \gamma = -\frac{\sin \theta'}{\sin \beta} \sin(\phi' - \phi). \quad (26)$$

The choice of the sign of β is arbitrary, but the sign of the other angles depend on this original choice. As we need to compute the inverse of the above trigonometric identities we have decided to use the inverse of the tangent function to improve numerical stability, taking care of the signs to recover the correct α and γ angles in the range $[-\pi; \pi]$.

The probability distribution of the complex field $P(\hat{n}_0)$ given the other value of this field in the direction \hat{n}_i , $i = 1 \dots N$, is as in Section 2.1,

$$\begin{aligned}
\mathcal{P}(P(\hat{n}_0)|P(\hat{n}_1), \dots, P(\hat{n}_N)) &= \\
&\sqrt{\frac{W_{0,0}}{2\pi}} \exp\left(-\frac{W_{0,0}}{2} |P(\hat{n}_0) - \bar{P}|^2\right), \quad (27)
\end{aligned}$$

with

$$\bar{P} = W_{0,0}^{-1} \sum_{i=1}^N W_{0,i}^* P(\hat{n}_i). \quad (28)$$

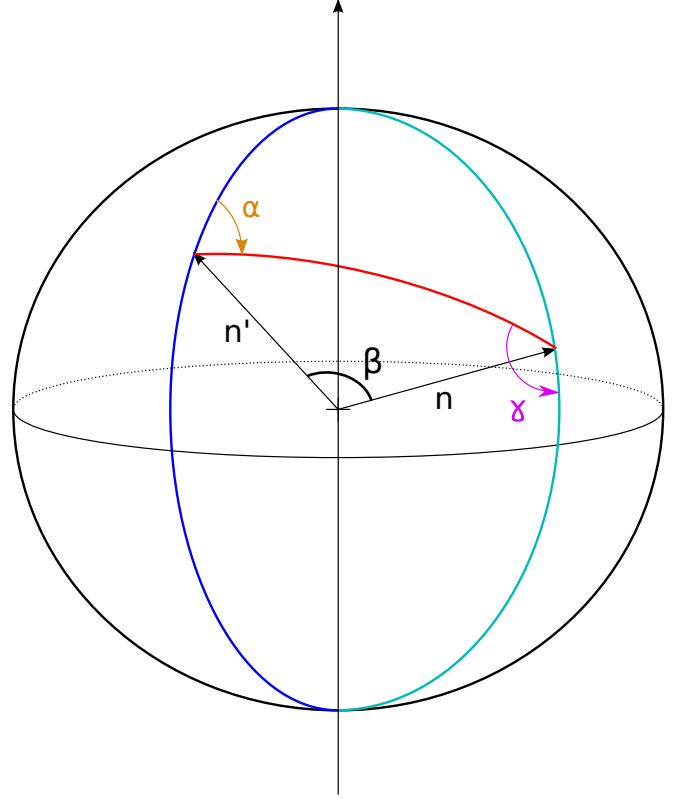


Figure 2. *Euler angle convention* – We represent here the conventions used for the orientation and the value of the Euler angles used in Eq. (19).

The Equations (12), (13) and (14) are still valid but this time for complex matrices and vectors. In that case A^\dagger is the conjugated transpose of matrix A . The resulting equation for the interpolated value $\tilde{P}(\hat{n})$, taken to be \bar{P} is

$$\tilde{P}(\hat{n}) = \sum_{i,j=1}^N S_{i,j}^{-1} \frac{\langle P(\hat{n})P^*(\hat{n}_i) \rangle}{{}_s \zeta(0, 0, 0)} P(\hat{n}_i), \quad (29)$$

with S as defined above in this Section. The variance of the interpolated value is

$$\begin{aligned}
\sigma_{\tilde{P}}^2(\hat{n}) &= {}_s \zeta(0, 0, 0) \times \\
&\left(1 - \sum_{i,j=1}^N S_{i,j}^{-1} \frac{\langle P(\hat{n})P^*(\hat{n}_i) \rangle \langle P(\hat{n}_j)P^*(\hat{n}) \rangle}{{}_s \zeta(0, 0, 0)^4}\right). \quad (30)
\end{aligned}$$

In the following, we focus on the actual implementation of the interpolation algorithm which uses the above two equations to compute the interpolated value in any direction.

2.3. Identifying neighbors

To be fast, the interpolation procedure must rely on a limited number of pixels, and more particularly the pixels just in the immediate vicinity of the direction of interpolation, using those pixels which carry most of the information about the interpolated point.

We discuss here a particular implementation to identify neighbors that relies on the HEALPIX framework. We use a method that relies on the use of the `neighbors()` function, which returns the immediate nine neighbors,

original N_{side}	target N_{side}	ℓ	Neighbors	Precision	Computational time (serial, minutes)	Memory (Megabytes)	HEALPIX time (serial, minutes)
1,024	2,048	4,096	9	2×10^{-2}	0.8	440	2.7
1,024	2,048	4,096	36	1×10^{-2}	5.1	5,500	2.7
2,048	4,096	4,096	9	3×10^{-3}	3.3	1,700	5.5
2,048	4,096	4,096	36	3×10^{-4}	19	22,000	5.5
4,096	8,192	4,096	9	4×10^{-4}	14	6,800	12

Table 1
Performance for maps supersampling

We give here the computing performance of our method to interpolate a scalar field containing power up to a bandlimit of $\ell = 4,096$. The computational time corresponds to the single processor wall time taken by the algorithm to interpolate the map at the given resolution from a map at N_{side} to a map at $2 \times N_{\text{side}}$. The HEALPIX computational time is estimated on the spherical harmonic synthesis transform at the target N_{side} resolution. The memory consumption gives the size of the pixelization cache in Random Access Memory. The precision corresponds to the square root of the average variance of the error predicted by FLINTS, this square root is divided by the standard deviation of the maps. The quoted serial times have been measured on an Intel Xeon E5410 2.33 GHz based computer. The standard deviation of the maps is $39 \mu\text{K/K}$.

sorted geometrically, see Fig. 1. The time complexity of `neighbors()` is constant both in the NESTED or RING mode of HEALPIX.

A fast way of extending this algorithm to a higher number of neighbors consists in using the NESTED mode of HEALPIX. This extension has already been described in Wandelt et al. (1998). We only consider here the neighbors symmetric according to the direction in which to interpolate in the NESTED tree sense. The neighbors at a level $y \geq 1$ in a map at resolution N_{side} can be found using a pixelization at N_{side}/y . Their number is then $9 \times 4^{y-1}$. We derive their identifiers in NESTED mode by computing the first neighbors using the function `neighbors()` of HEALPIX at resolution N_{side}/y . We shift the bits of these identifiers by $2(y-1)$ and fill up the lower bits with all the possible combinations. This procedure yields all the $9 \times 4^{y-1}$ pixel neighbors of a given direction.

This procedure is more attractive given our computational constraints than using the alternative procedure `query_disc()`: it allows a stable number of pixels per neighbors, their geometrical distribution according to the central direction is stable and insensitive to numerical rounding errors, which makes it easier to tabulate S^{-1} and it is relatively fast to compute the list. For these reasons, we only use this procedure in the rest of this work.

2.4. Tabulating S^{-1}

To reduce the time needed to compute the interpolation, we tabulate the matrices S^{-1} for all possible central pixels (corresponding to T_5 in the Figure 1). This means we would need to precompute and store a matrix for each pixel of the map to interpolate. We made use of the symmetries of the HEALPIX pixelization to reduce this cost. As there is a rotational invariance in the equatorial part of the pixelization, it suffices to store one pixel per ring. For the polar regions, it would be sufficient to store the weights for only one quarter of one of the HEALPIX base tiles, since there is an eight-fold rotational invariance and an additional north-south symmetry. Using all these symmetries would reduce the amount of memory required to store the precomputed weights by nearly $1/48$.

For our implementation we use a subset of these symmetries since there is a trade-off between reduction of memory use and the implementation complexity for the

required pixel permutations. In addition to the equatorial symmetry, we use the north-south symmetry for the case of the spin-0 field only. Memory use scales as $O(N_{\text{ngb}}^2 \times N_{\text{side}}^2)$, with N_{ngb} the number of neighbors chosen for computing the interpolation.

To compute S^{-1} itself from S , we use the Cholesky decomposition of $S = {}^tLL$ and do a direct inversion of L . We used the algorithm described in Press et al. (1992). As the matrix S becomes so ill-conditioned that the Cholesky decomposition fail for high resolution map, we introduce an additional term n to help at computing this decomposition when this term is required. So, in practice, we decompose $S + n\mathcal{I}$ instead of S . By construction, the value of n is much smaller than one. If n is too big, the interpolation error is larger than it should. If n is too small, the decomposition fails. We use for n a value given by

$$n = -\lambda_{\text{min,negative}} + \epsilon_{\text{precision}} \quad (31)$$

where $\lambda_{\text{min,negative}}$ is the lowest negative eigenvalue of S at the used precision, $\epsilon_{\text{precision}}$ is a quantity dependent on the machine precision used for doing the actual computation on S . For double-precision, we take $1.49 \cdot 10^{-8}$, which is the square root of the smallest deviation from 1.0 detectable in a double precision representation.

2.5. The interpolation algorithm

Finally, the interpolation algorithm consists in achieving the following steps:

1. We set the resolution of the map to interpolate at N_{side} and the band width to ℓ_{max} .
2. We start by tabulating according to $\beta \in [0, \pi]$ the $\zeta(0, \beta, 0)$ function, defined in Eq. (19).
3. For the HEALPIX pixelization at N_{side} , we compute S using Eq. (20), invert it and tabulate it according to Section 2.4. This is the end of the preparation phase.
4. For any direction (θ, ϕ) , we compute the identifiers of the pixel neighbors according to Section 2.3.
5. We sum up the value of the field sampled at those pixels and weighed them according to Eq. (29).
6. If required by the user, we also compute the error in the interpolation using Eq. (30).

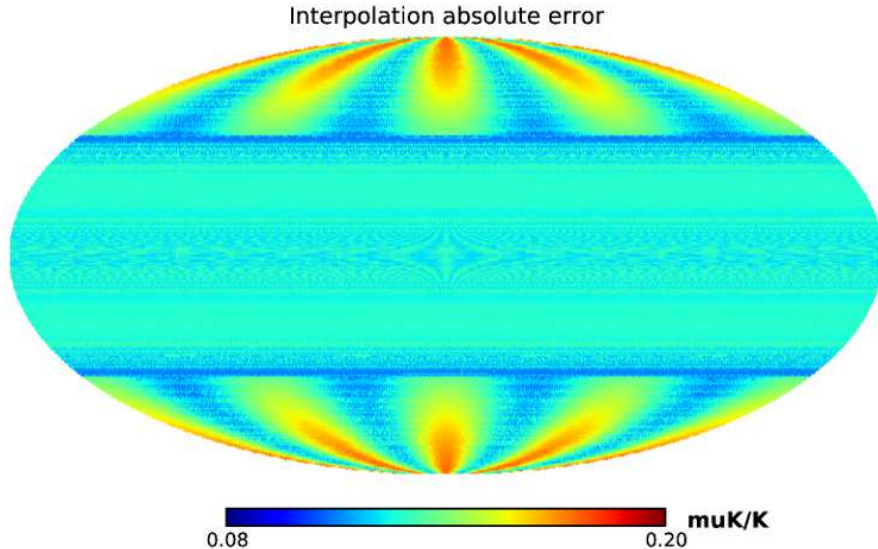


Figure 3. *Spatial distribution of predicted interpolation error for the upsampling* – We show the distribution of the error predicted by the algorithm for each interpolated pixel of the sky. We predict a map at $N_{\text{side}} = 4,096$ from a map at $N_{\text{side}}/2 = 2,048$, with $\ell_{\text{max}} = 4,096$. The structure of the error distribution reflects the features of the HEALPIX pixelization.

In all the subsequent tests, we have used the above scheme to generate the interpolated values.

2.6. Supersampling interpolation performance

We test the interpolator by supersampling a CMB map to twice the original resolution. Please refer to the results in Table 1 and in Figure 3. In all these tests, we start from a map at a resolution of N_{side} and predict its values at twice the resolution, $2 \times N_{\text{side}}$. Note that all these test are done for fixed bandlimit $\ell = 4,096$ while the resolution of the grid is varied. For the lowest starting resolution of $N_{\text{side}} = 1,024$ the field is somewhat undersampled, since modes beyond $\ell = 2N_{\text{side}}$ begin to be noticeably aliased on the HEALPIX grid. Owing to the hierarchical property of the HEALPIX grid, the higher resolution pixels tile the lower resolution pixels. The distance from the members of the interpolation stencil is therefore one fourth or three fourth of the size of a pixel. Based on numerical experiments we estimate the worst case error for directions farthest away from the members of the interpolation stencil to be no more than 50% higher than shown in Figure 3.

In Figure 3, the distribution of the interpolation error reflects the features of the HEALPIX pixelization. The error is uniformly small in the equatorial regime and shows the symmetries of the pixelization in the northern and southern caps.

We tabulate the supersampling precision and the time consumption in Table 1. For comparison we list the time required to compute a single HEALPIX transform from $\{a_{lm}\}$ space to pixel space. The two operations take roughly the same time. Note that the spherical harmonic transform has only been done one way, whereas the interpolation starts from pixels and yields pixels. As expected the error decreases with increased resolution and number of neighbors. It is interesting to see that we may get a decrease of one magnitude in the error by changing the number of neighbors at the resolution $N_{\text{side}} = 2,048$. Doing the same exercise with $N_{\text{side}} = 4,096$ yields a large

number of degeneracies in the S matrices. That shows that we reach the level where the problem of interpolation is dominated by errors in the floating point representation, as expected since a HEALPIX map at resolution N_{side} is able to encode wavenumbers up to $\ell \sim 2N_{\text{side}}$. So, as our ℓ_{max} is 4,096 here, a map at $N_{\text{side}} = 2,048$ can be interpolated at high precision with a sufficient number of neighbors.

3. APPLICATION TO CMB LENSING

In this section, we focus on the use of our interpolation procedure for producing lensed maps of the CMB. In Section 3.1, we recall the basic lensing equation in the Born approximation and the notation. In Section 3.2, we compare the predictive performance of FLINTS to LENSPIX and to the naive technique in HEALPIX. Finally, in Section 3.3, we compare the power spectra of the lensed temperature and polarization as obtained through FLINTS and using CAMB.

3.1. Theory of lensing

Gravitational lensing acts like a remapping of the CMB photons on the sky. Thus the temperature signal on the sky is given by

$$T_{\text{observed}}(\hat{\mathbf{n}}) = T_{\text{CMB}}(\hat{\mathbf{n}} + \mathbf{d}(\hat{\mathbf{n}})), \quad (32)$$

where T_{observed} is the observed temperature of the CMB in the direction $\hat{\mathbf{n}}$, T_{CMB} is the unlensed primary signal, and $\mathbf{d}(\hat{\mathbf{n}})$ is the deflection field. This relation is also true for the polarization field defined by

$$P(\hat{\mathbf{n}}) = Q(\hat{\mathbf{n}}) + iU(\hat{\mathbf{n}}) \quad (33)$$

with Q and U the Stokes parameters, with P being a spin-2 field.

The deflection field defines in what direction and by what angle the photons were deflected from their original position. In the local basis defined by the direction $\hat{\mathbf{n}}$, we may define the angle $\alpha(\hat{\mathbf{n}})$ as

$$\mathbf{d}(\hat{\mathbf{n}}) \propto \cos(\alpha)\mathbf{u}_\theta(\hat{\mathbf{n}}) + \sin(\alpha)\mathbf{u}_\phi(\hat{\mathbf{n}}) \quad (34)$$

N_{side}	FLINTS					TORUS	ECP(LENXPix)			
	Init. time (minutes)	Interp. time (minutes)	Total time (minutes)	Precision L_2	Precision L_∞	Total time (minutes)	Interp. time (minutes)	Total time (minutes)	Precision L_2	Precision L_∞
1,024	8	1	8	2%	11%	32	5.0	9	5%	24%
2,048	9	6	20	0.3%	2.65%	~160-250*	12	20	9%	125%
4,096	16	22	51	0.04%	0.3%	~640-1,000*	34	52	7.5%	127%

Table 2
Lensing performance

NB: Numbers with * are extrapolated from table 3 of Basak et al. (2009). “Interp.” stands for “Interpolation”. “Init.” stands for “Initialization”. We measure the time for producing a lensed map, temperature and polarization, from a random realization of the CMB fluctuations and of the lensing potential. The total time is the sum of the interpolation time, the time to make an unlensed healpix map, the time to compute the deflection map but not the initialization time given in the first column. The L_2 (L_∞) precision corresponds to the standard deviation (maximum absolute value) of the error distribution divided by the standard deviation of the simulated CMB map, which is $39 \mu\text{K}/\text{K}$. For all cases we used $\ell_{\text{max}} = 4,096$ and nine neighbors for FLINTS, and a interpolation factor of one for the ECP method in LENXPix. The maps at $N_{\text{side}} = 1,024$ were therefore undersampled.

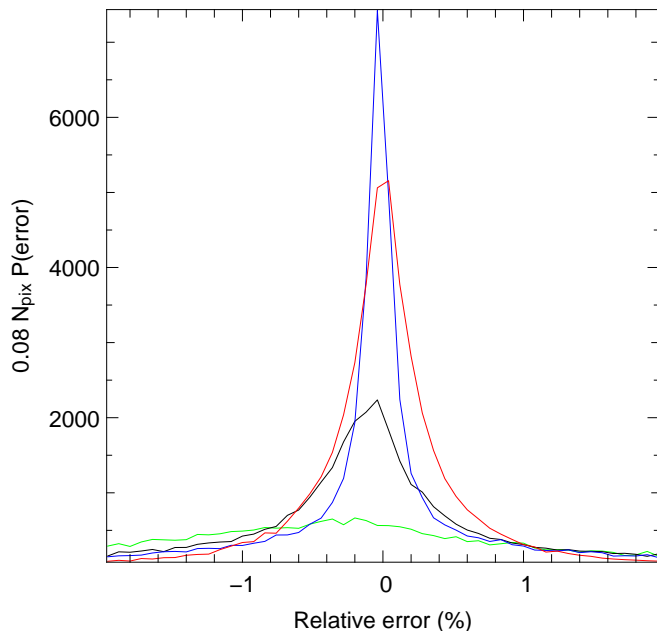


Figure 4. *Interpolated CMB vs True value* – Distribution of the error in the value given by both naive interpolation on a HEALPIX mesh and our method for different HEALPIX resolution. For each line, we represented the distribution of the relative difference between the actual interpolated value and the true value. The green, black and blue lines correspond to HEALPIX interpolation at $N_{\text{side}} = 2,048$, $N_{\text{side}} = 4,096$ and $N_{\text{side}} = 8,192$ respectively. The red line corresponds to our method at $N_{\text{side}} = 2,048$.

with $(\hat{n}, \mathbf{u}_\theta, \mathbf{u}_\phi)$ the local spherical orthonormal basis, with $\mathbf{u}_\theta = \partial\hat{n}/\partial\theta$ and $\mathbf{u}_\phi = \partial\hat{n}/\partial\phi$. In this basis, the lensed direction \hat{n}' may be written as

$$\hat{n}' = \hat{n} + \mathbf{d}(\hat{n}) = \cos(|d|)\hat{n} + \sin(|d|)\cos(\alpha)\mathbf{u}_\theta + \sin(|d|)\sin(\alpha)\mathbf{u}_\phi. \quad (35)$$

We prefer this form of the lensed direction instead of using the angles for numerical stability, at the cost of computing a few additional trigonometric function. Using the direct angle relation, as in e.g. Basak et al. (2009), may expose us to problems in the case of directions near the poles. The displacement field $\mathbf{d}(\hat{n})$ is obtained by taking the spherical gradient of a scalar potential, corresponding to the projected gravity field in the Born approximation.

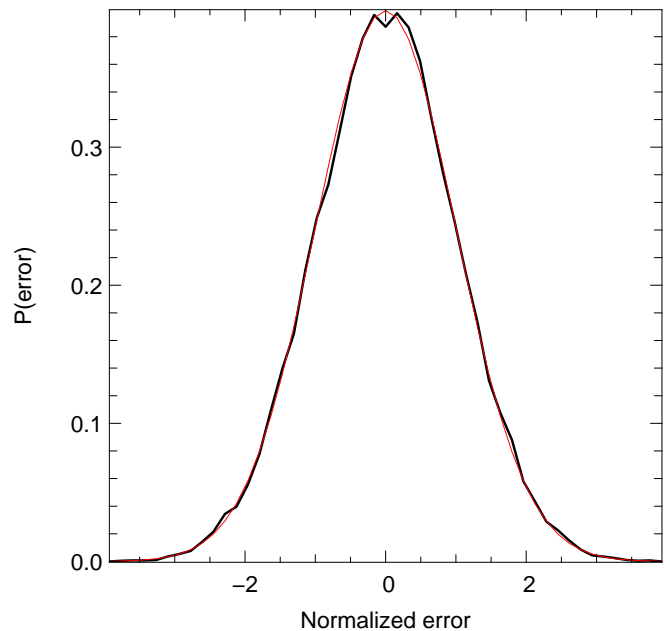


Figure 5. *Accuracy of the error estimate* – The thick black line shows the measured error normalized using the error estimate, Eq. (16), at each pixel. The overlotted thin red line is a Gaussian distribution of width 1 and centered on 0 showing perfect agreement between predicted and actual error.

3.2. Test of producing lensed CMB maps

We now test our procedure for generating precise lensed CMB maps. We compare our generated maps to:

- the true lensed maps, obtained by summing exactly the spherical harmonics at the position of interpolation
- the naive interpolation procedure using a simple bilinear interpolation of CMB maps simulated at high resolution. This algorithm is included in the HEALPIX package for visualization purposes and was not intended for scientific use, but it is still useful as a point of comparison to assess whether a more complicated interpolation procedure is warranted.
- the ECP bicubic interpolation algorithm implemented in LENXPix. This is the current mainstream algorithm for quickly computing lensed

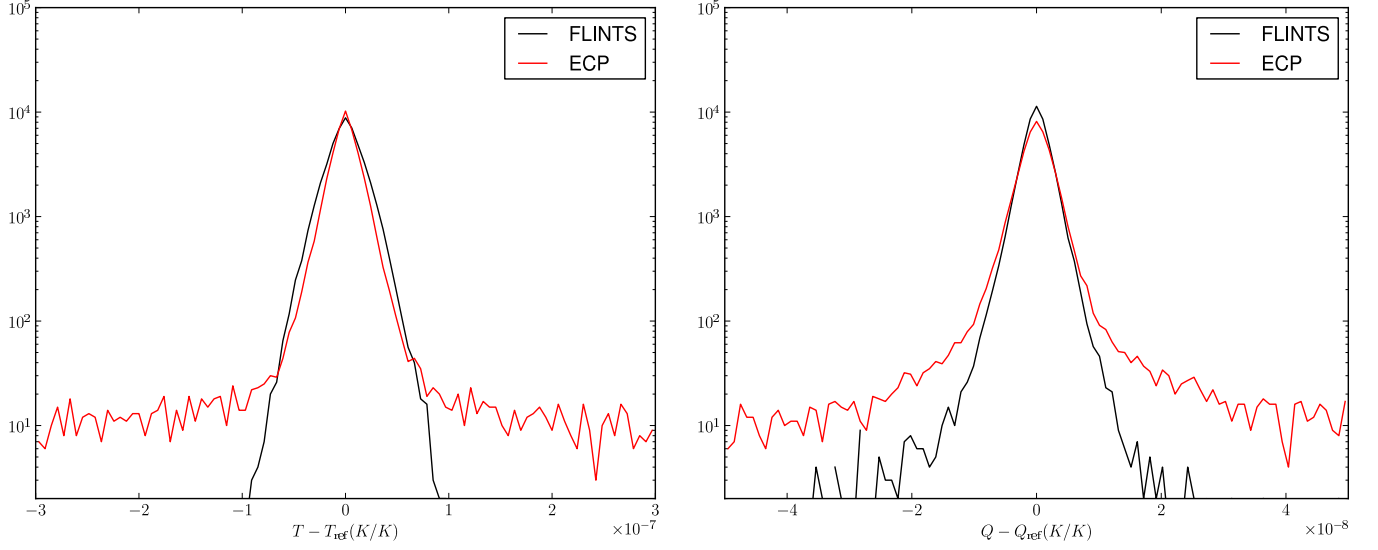


Figure 6. *Error distribution of the Equicylindrical projection interpolation and of FLINTS* – We represent the measured error distribution of the temperature (T , left panel) and one plane of polarization (Q , right panel) map. We use $N_{\text{side}} = 4,096$ and $\ell_{\text{max}} = 4,096$ and no multiplication factor for the ECP method. The error distribution is computed by taking the difference of the value predicted by the interpolator to the exact value computed using ECP method. In black (red) solid line, we represent the error distribution of our FLINTS (ECP interpolation) algorithm.

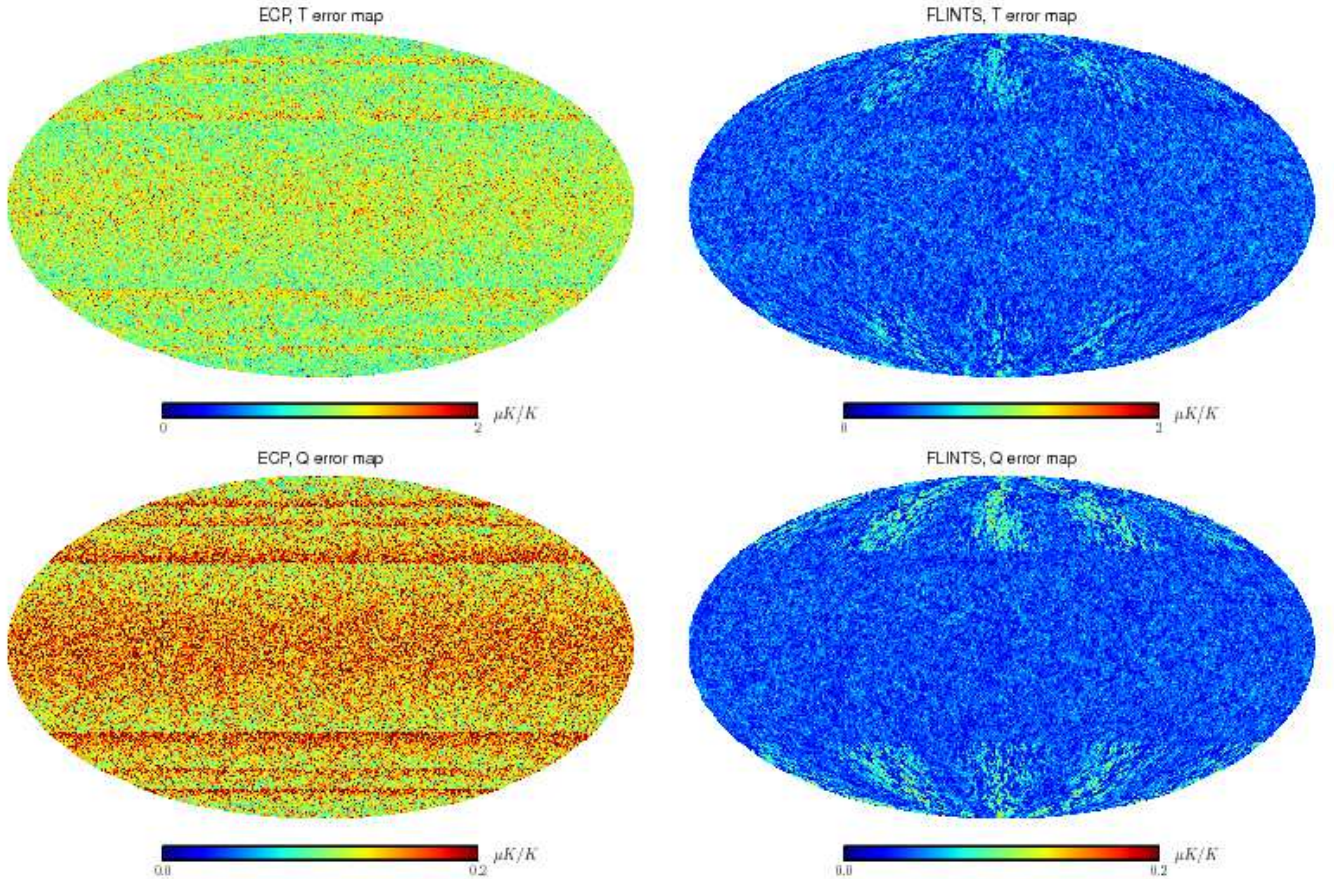


Figure 7. *Error distribution of the Equi-cylindrical projection interpolation and of FLINTS on the sky* – We represent a comparison of the error distribution on the sky of the interpolated temperature (T , top panels) and one polarization plane (Q , bottom panels) map. The errors in the ECP interpolation, are represented in the left panels. The errors of the FLINTS interpolation are represented in the right panels. We compare to the exact lensing method. All maps were computed at $N_{\text{side}} = 1,024$, with $\ell_{\text{max}} = 2,048$. For visualization purposes, we degraded the error maps to a resolution of $N_{\text{side}} = 128$.

maps.

As it is very expensive to compute the true lensed map on the full sky we limit ourselves to testing our method on a restricted subset of pixels distributed uniformly over the sky. More specifically we chose directions on the sky at a resolution of $N_{\text{side}} = 64$ (49152 pixels).

We show the result in Fig. 4. We note that FLINTS behaves much better than the naive interpolation. Our interpolation procedure, executed at a resolution of N_{side} is able to match fairly well with the naive interpolation used at $4N_{\text{side}}$. This matches Lewis (2005) who indicated that one needs at least 16 times more pixels than the base CMB map to produce acceptable spectrum using a naive interpolation procedure.

Moreover, the tails of the error distributions of the interpolated field are much more Gaussian, as illustrated in Fig. 5. There, we represented the error normalized by the expected standard deviation given by Eq. (16). If the errors are Gaussian with exactly this deviation, we must obtain a Gaussian of standard deviation equal to one, which is exactly what we obtain.

In Table 2, we compare the performances of our method, FLINTS, with the method described in Basak et al. (2009), labelled TORUS, and the ECP interpolation implemented in LENSPIX. For FLINTS and ECP we give an estimate of the attained precision. We also measure the time required to produce one lensed map. We note that the precision is better for FLINTS than for ECP. The problem for ECP are the heavy tails in the error distribution, as shown in Fig. 6. Furthermore, at low N_{side} fixed ℓ_{max} , the field fluctuations are undersampled which degrades the predictive properties of ECP method. On the other hand, FLINTS keeps errors lower because it takes into account the underlying fluctuations through the use of the angular power spectra in the weights. At $N_{\text{side}} = 4,096$, the central part of the error distribution represented in Fig. 6 is the same showing convergence of the two methods.

A comparison of the differences in the spatial distribution of the interpolation errors of the ECP and FLINTS method are given in Fig. 7. We represent there the sky distribution of the errors in the lensed temperature and polarization maps. We compute the reference maps using the full resummation of the spherical harmonics at the displaced positions. The maps are computed at a resolution $N_{\text{side}} = 1,024$, $\ell_{\text{max}} = 2,048$, with an oversampling factor equal to one for the ECP method. We note that the error distribution of the ECP interpolation is linked to the projection of the ECP mesh onto an HEALPIX mesh. On the other hand, the FLINTS interpolation is essentially tracking the shape of the HEALPIX grid, as already seen in Fig. 3. As in Fig. 6, the overall amplitude of error of the ECP interpolation is larger than the one given by the FLINTS interpolation.

The total time for both methods is similar but FLINTS has initialization time overhead for precomputing S^{-1} (Section 2.4). This overhead may still be further optimized by using more of the symmetries of HEALPIX pixelization. Overall, FLINTS is more precise than ECP by order of magnitude for simulations resembling data from a high resolution CMB polarization mission. Both of these methods are much faster than the TORUS method.

3.3. Lensed power spectra

As an additional test of the precision of our method we compare the power spectra of our lensed temperature and polarization maps with the theoretical predictions from CAMB (Lewis et al. 2000; Challinor & Lewis 2005). We show the difference of the average spectrum of 350 lensed maps and the unlensed spectrum in Figure 8.

We tested how our method fared compared to naive temperature interpolation and on a limited number of exactly interpolated pixels. We now check the interpolation of both the temperature and the polarization fields on different scales by considering the difference between the lensed spectra, $C_{\ell,\text{lensed}}^{TT}$ and the unlensed spectra. To assess the precision of our procedure, we use the spectra computed by CAMB (Lewis et al. 2000; Challinor & Lewis 2005) as a reference. The results, given as the difference of the lensed spectra to the unlensed spectra, are given in Figure 8. We used $N_{\text{side}} = 4,096$ and $\ell_{\text{max}} = 5,000$ as an input to FLINTS. The CAMB spectra were predicted using $\ell_{\text{max}} = 10,000$ and $k_{\eta,\text{max}} = 100,000$ in very high accuracy mode. We also show the relative difference between our spectra and CAMB spectra. We see that the difference between the two does not exceed 0.5% statistically at $\ell = 3,000$. While the B-mode spectrum has a small but systematic excess of power of about 0.1 – 0.2% in our measured BB compared to the prediction given by CAMB, we note that this is of the same order as the advertised accuracy CAMB even in high-precision mode (Challinor & Lewis 2005). In addition, CAMB is not guaranteed to be accurate at this level beyond $\ell \sim 2000$, so the comparison breaks down at this point and it is not clear whether CAMB or FLINTS is more accurate.

In any case, the interpolation accuracy is more than sufficient for practical purposes in all cases. To illustrate, we display the cosmic variance range for the temperature power spectrum in the first panel of Figure 8. This shows the unavoidable error in the estimation of C_{ℓ} from a perfect, all-sky, unlensed map. For the very small B-mode signal these numerical errors will remain much smaller than measurement error for the foreseeable future.

4. CONCLUSION

For a given interpolation stencil, we describe the optimal interpolation technique for isotropic band-limited fields of arbitrary spin, sampled on the sphere. Taking advantage of the symmetry properties of the HEALPIX pixelization, the method is fast and memory-efficient. To test this approach we implement a supersampling filter for HEALPIX temperature and polarization maps. A Monte Carlo study confirms both the predicted precision and our estimates of memory and CPU time scaling.

We demonstrate this interpolation method to be powerful tool to simulate lensed CMB temperature and polarization maps from unlensed maps. Our Monte Carlo comparison to exact reference maps computed by LENSPIX and to predicted lensed power spectra by CAMB demonstrate that we achieve an accuracy which exceeds the requirements of the PLANCK data (The Planck Collaboration 2006) while reducing the required computational time by an order of magnitude compared to using, e.g., the Torus method. In addition, the method allows very easy parallelization as the

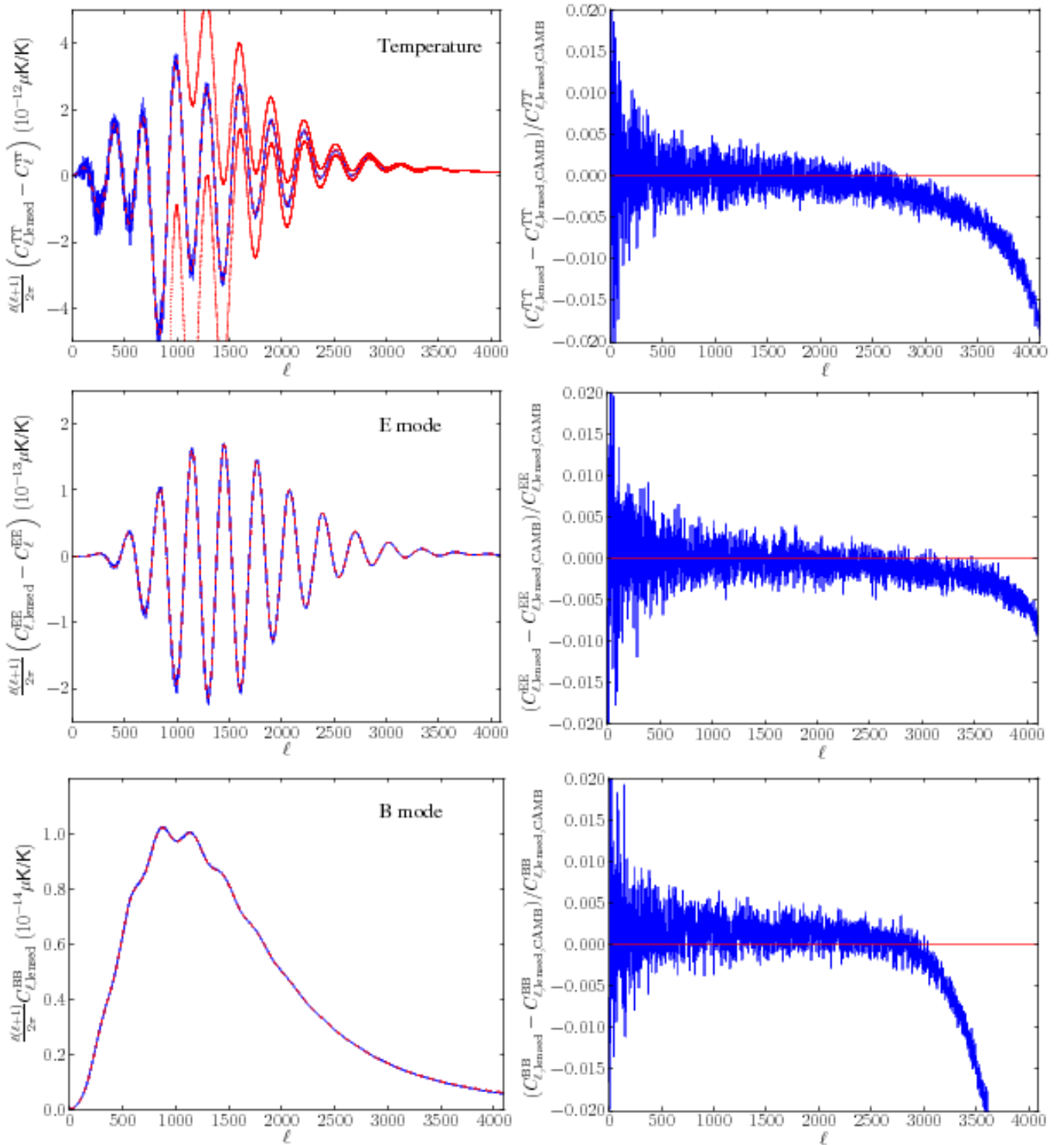


Figure 8. *Precision of lensed power spectra* – We show the differences between the lensed spectra and the unlensed spectra for ~ 350 realizations of CMB fluctuations and lensing potentials. In the left panels, the dashed, red line is the difference as computed by CAMB, and the solid, blue line the result obtained using our interpolation technique. Cosmic variance error bars are shown as a dotted line in the top-left most panel. In the right panels, we represented the relative difference between the CAMB prediction and FLINTS prediction. We represented the change in the C_ℓ for the temperature (top row), the E polarization mode (middle row), the B polarization mode (bottom row). The fluctuations are here normalized by the CMB temperature and are unitless. The red lines in the right panels represent perfect agreement with CAMB. The lensed maps were computed using a CMB map at $N_{\text{side}} = 4,096$, $\ell_{\text{max}} = 5,000$ and 9 neighbors.

procedure is strictly local in pixel space. We compared the performance and the precision of our method to the Equi-cylindrical projection interpolation method. The two methods have similar speed. FLINTS is more precise and has no catastrophic errors.

We conclude that this method is a very promising technique in terms of speed, precision and scalability for the simulation of high resolution maps of the lensed CMB temperature and polarization anisotropies. FLINTS enables us to produce lensed maps as cheaply as making a spherical harmonic transform, and makes us capable of producing thousands of simulations of the lensed sky within an acceptable computational time. This advance may allow us to run a full likelihood analysis of the lensing potential in observed CMB data with current computer technology, which is not possible with other known methods of computing lensed maps.

ACKNOWLEDGMENTS

We thank the Planck group at JPL and the astrophysics group at Caltech for their hospitality while this work was begun. We thank S. Prunet for comments on the first version of the draft. We acknowledge financial support from NSF Grant AST 07-08849. GL acknowledges grant from the the ‘‘Programme visiteur de l’IAP’’ and financial support from French ANR (OTARIE). This research was supported in part by the National Science Foundation through TeraGrid resources provided by the NCSA under grant number [TG-MCA04N015]. Teragrid systems are hosted by Indiana University, LONI, NCAR, NCSA, NICS, ORNL, PSC, Purdue University, SDSC, TACC and UC/ANL. The authors thank the anonymous referee for his/her constructive remarks.

REFERENCES

Abazajian, K. N., & Dodelson, S. 2003, Phys. Rev. Lett., 91, 041301
 Basak, S., Prunet, S., & Benabed, K. 2009, A&A, 508, 53, arXiv:0811.1677
 Challinor, A., & Lewis, A. 2005, Phys. Rev. D, 71, 103010, arXiv:astro-ph/0502425
 Condon, E. U., & Shortley, G. 1951, The Theory of Atomic Spectra (Cambridge University Press)
 Das, S., & Bode, P. 2008, ApJ, 682, 1, 0711.3793
 Edmonds, A. R. 1957, Angular Momentum in Quantum Mechanics (Princeton University Press)
 Goldberg, J. N., Macfarlane, A. J., Newman, E. T., Rohrlich, F., & Sudarshan, E. C. G. 1967, Journal of Mathematical Physics, 8, 2155

Górski, K. M., Hivon, E., Banday, A. J., Wandelt, B. D., Hansen, F. K., Reinecke, M., & Bartelmann, M. 2005, ApJ, 622, 759, arXiv:astro-ph/0409513
 Hamilton, J., & Charlassier, R. 2010, in EAS Publications Series 40, Third ARENA Conference on ‘‘An Astronomical Observatory at CONCORDIA (Dome C, Antarctica)’’, ed. L. Spinoglio & N. Epchtein, 399, EDP Sciences
 Hamimeche, S., & Lewis, A. 2008, Phys. Rev. D, 77, 103013, 0801.0554
 Hirata, C. M., Ho, S., Padmanabhan, N., Seljak, U. c. v., & Bahcall, N. A. 2008, Phys. Rev. D, 78, 043520
 Hirata, C. M., Padmanabhan, N., Seljak, U., Schlegel, D., & Brinkmann, J. 2004, Phys. Rev. D, 70, 103501, astro-ph/0406004
 Hu, W., & White, M. 1997, Phys. Rev. D, 56, 596, astro-ph/9702170
 Kaplinghat, M., Knox, L., & Song, Y.-S. 2003, Phys. Rev. Lett., 91, 241301
 Kesdaen, M., Cooray, A., & Kamionkowski, M. 2002, Phys. Rev. Lett., 89, 011304
 Knox, L., & Song, Y.-S. 2002, Phys. Rev. Lett., 89, 011303
 Lesgourgues, J., Perotto, L., Pastor, S., & Piat, M. 2006, Phys. Rev. D, 73, 045021
 Lewis, A. 2005, Phys. Rev. D, 71, 083008, arXiv:astro-ph/0502469
 Lewis, A., Challinor, A., & Lasenby, A. 2000, Astrophys. J., 538, 473, arXiv:astro-ph/9911177
 McMahon, J. J., et al. 2009, in The Thirteenth International Workshop on Low Temperature Detectors, ed. B. Young, B. Cabrera, & A. Miller, Vol. 1185 (AIP), 511–514
 Newburgh, L. B., et al. 2005, in Bulletin of the American Astronomical Society, Vol. 37, Bulletin of the American Astronomical Society, 1429–+
 Newman, E. T., & Penrose, R. 1966, Journal of Mathematical Physics, 7, 863
 Press, W., Teukolsky, S., Vetterling, W., & Flannery, B. 1992, Numerical Recipes in C, 2nd edn. (Cambridge, UK: Cambridge University Press)
 Smith, K. M., Hu, W., & Kaplinghat, M. 2006a, Phys. Rev. D, 74, 123002
 Smith, K. M., Zahn, O., & Doré, O. 2007, Phys. Rev. D, 76, 043510
 Smith, S., Challinor, A., & Rocha, G. m. c. 2006b, Phys. Rev. D, 73, 023517
 The Planck Collaboration. 2006, arXiv:astro-ph/0604069
 Trapani, S., & Navaza, J. 2006, Acta Crystallographica Section A, 62, 262
 Wandelt, B. D., Hivon, E., & Gorski, K. M. 1998, in Fundamental Parameters in Cosmology, ed. J. Tran Thanh Van, arXiv:astro-ph/9803317, proceedings of the XXXIIIrd Rencontres de Moriond
 Wiener, N. 1949, Extrapolation, Interpolation, and Smoothing of Stationary Time Series (MIT Press)
 Zaldarriaga, M., & Seljak, U. 1997, Phys. Rev. D, 55, 1830, arXiv:astro-ph/9609170

APPENDIX

A. SPIN-WEIGHTED SPHERICAL HARMONIC

Spin s functions ${}_s f$ transform under a locally planar rotation $R(\theta)$ about the direction \hat{n} as

$${}_s f(R(\theta)\hat{n}) = e^{is\theta} {}_s f(\hat{n}) \quad (\text{A1})$$

On the sphere, these functions may be expanded on the spin- s spherical harmonic basis ${}_s Y_{\ell,m}(\hat{n})$ as (Newman & Penrose 1966; Goldberg et al. 1967; Zaldarriaga & Seljak 1997)

$${}_s f(\hat{n}) = \sum_{\ell=0}^{+\infty} \sum_{m=-\ell}^{+\ell} {}_s f_{\ell,m} [{}_s Y_{\ell,m}(\hat{n})]. \quad (\text{A2})$$

As for spin-0 function, the spherical harmonic coefficient ${}_s f_{\ell,m}$ may be obtained using

$${}_s f_{\ell,m} = \int_{S^2} d\Omega(\hat{n}) [{}_s Y_{\ell,m}(\hat{n})]^* {}_s f(\hat{n}) \quad (\text{A3})$$

with S^2 being the sphere in dimension three. The spin-weighted spherical harmonic function may be expressed directly from the Wigner rotation matrices: (Goldberg et al. 1967)

$${}_s Y_{\ell,m}(\hat{n}) = {}_s Y_{\ell,m}(\theta, \phi) = \sqrt{\frac{2\ell+1}{4\pi}} D_{-s,m}^{\ell}(\phi, \theta, 0) \quad (\text{A4})$$

where we used the Condon-Shortley phase (Condon & Shortley 1951) convention, θ and ϕ are respectively colatitude and longitude on the sphere. The Wigner D matrix $D_{m,m'}^{\ell}$ may be further expanded with the help of the Wigner d function

$$D_{m,m'}^{\ell}(\phi, \theta, \rho) = e^{-im\phi} d_{m,m'}^{\ell}(\theta) e^{-im'\rho} \quad (\text{A5})$$

which yields

$${}_s Y_{\ell,m}(\hat{n}(\theta, \phi)) = (-1)^s \sqrt{\frac{2\ell+1}{4\pi}} e^{im\phi} d_{m,-s}^{\ell}(\theta). \quad (\text{A6})$$

Furthermore, we recall the spin- s spherical harmonic addition relation (e.g. Hu & White 1997)

$$\sum_{m=-\ell}^{+\ell} [{}_{s'} Y_{\ell,m}^*(\theta', \phi')] [{}_s Y_{\ell,m}(\theta, \phi)] = \left(\frac{2\ell+1}{4\pi}\right) \sum_{m=-\ell}^{+\ell} D_{-s',m}^{\ell*}(\phi', \theta', 0) D_{-s,m}^{\ell}(\phi, \theta, 0) \quad (\text{A7})$$

$$= \left(\frac{2\ell+1}{4\pi}\right) D_{-s,-s'}^{\ell}(\alpha, \beta, \gamma) \quad (\text{A8})$$

$$= \sqrt{\frac{2\ell+1}{4\pi}} e^{-is\gamma} {}_s Y_{\ell,-s'}(\beta, \alpha) \quad (\text{A9})$$

$$(\text{A10})$$

with (α, β, γ) the Euler angles of the rotation bringing the direction (θ', ϕ') to (θ, ϕ) .

B. COMPUTING THE WIGNER D FUNCTION

We use the decomposition of the Wigner d function in terms of their Fourier representation. This decomposition is taken from Edmonds (1957). We start by factorizing a nodal rotation:

$$R(0, \beta, 0) = R\left(-\frac{\pi}{2}, 0, 0\right) R\left(0, -\frac{\pi}{2}, 0\right) R(\beta, 0, 0) R\left(0, \frac{\pi}{2}, 0\right) R\left(\frac{\pi}{2}, 0, 0\right). \quad (\text{B1})$$

Expressing this matrix multiplication in terms of the elements of the D matrices yields the identity:

$$d_{m_1, m_2}^{\ell}(\beta) = i^{m_2 - m_1} \sum_{n=-\ell}^{\ell} d_{n, m_1}^{\ell}\left(\frac{\pi}{2}\right) d_{n, m_2}^{\ell}\left(\frac{\pi}{2}\right) e^{in\beta}. \quad (\text{B2})$$

If we let $\Delta_{m_1, m_2}^{\ell} = d_{m_1, m_2}^{\ell}\left(\frac{\pi}{2}\right)$ and $B_{n, m_1, m_2}^{\ell} = i^{m_1 - m_2} \Delta_{n, m_1}^{\ell} \Delta_{n, m_2}^{\ell}$, then we see explicitly the expression of $d_{m_1, m_2}^{\ell}(\beta)$ in terms of a discrete Fourier transform:

$$d_{m_1, m_2}^{\ell}(\beta) = \sum_{n=-\ell}^{\ell} B_{n, m_1, m_2}^{\ell} e^{in\beta}. \quad (\text{B3})$$

The recursive formula for d -matrix can be adapted for the specific case of $\beta = \pi/2$. This calculation yields the following recursion formula:

$$\Delta_{\ell, 0}^{\ell} = -\left(\frac{2\ell-1}{2\ell}\right)^{1/2} \Delta_{\ell-1, 0}^{\ell-1} \quad (\text{B4})$$

$$\Delta_{\ell, m_2}^{\ell} = \left[\frac{(\ell/2)(2\ell-1)}{(\ell+m_2)(\ell+m_2-1)}\right]^{1/2} \Delta_{\ell-1, m_2-1}^{\ell-1} \quad (\text{B5})$$

$$\begin{aligned} \Delta_{m_1, m_2}^{\ell} &= \frac{2m_2}{[(\ell-m_1)(\ell+m_1+1)]^{1/2}} \Delta_{m_1+1, m_2}^{\ell} \\ &\quad - \left[\frac{(\ell-m_1-1)(\ell+m_1+2)}{(\ell-m_1)(\ell+m_1+1)}\right]^{1/2} \Delta_{m_1+2, m_2}^{\ell} \end{aligned} \quad (\text{B6})$$

with an initial condition

$$\Delta_{0,0}^0 = 1. \quad (\text{B7})$$

We start by using Eq. (B4) to increase the order in ℓ from the initial condition. At the same time, we compute all $\Delta_{\ell,m}^\ell$ for $0 \leq m \leq \ell$ using Eq. (B5) recursively. At the end of the recursion we have access to all $\Delta_{\ell,m}^\ell$ at the required ℓ . We use the last equation (B6) to compute Δ_{u,m_1}^ℓ and Δ_{u,m_2}^ℓ for all $-\ell \leq u \leq \ell$ at m_1 and m_2 fixed.

The function $d_{m_1,m_2}^\ell(\beta)$ is used to compute the angular correlation function described in Eq. (19). We decided to tabulate and interpolate using cubics the correlation function. For performance reason, we compute the Wigner- d function at all β at sufficiently high resolution and then sum the contribution at each β for any given ℓ of the whole summation of $d_{-s,-s}^\ell$.